

A Josephson phase battery

Elia Strambini,^{1,*} Andrea Iorio,^{1,†} Ofelia Durante,² Roberta Citro,² Cristina Sanz-Fernández,³ Claudio Guarcello,^{2,3} Ilya V. Tokatly,⁴ Alessandro Braggio,¹ Mirko Rocci,¹ Nadia Ligato,¹ Valentina Zannier,¹ Lucia Sorba,¹ F. Sebastian Bergeret,^{5,‡} and Francesco Giazotto^{1,§}

¹*NEST, Istituto Nanoscienze-CNR and Scuola Normale Superiore, I-56127 Pisa, Italy*

²*Dipartimento di Fisica “E. R. Caianiello”, Università di Salerno, 84084 Fisciano (Salerno), Italy*

³*Centro de Física de Materiales (CFM-MPC), Centro Mixto CSIC-UPV/EHU, Manuel de Lardizabal 4, E-20018 San Sebastian, Spain*

⁴*Nano-Bio Spectroscopy group, Departamento de Física de Materiales, Universidad del País Vasco Av. Tolosa 72, E-20018 San Sebastian, Spain[¶]*

⁵*Donostia International Physics Center (DIPC), Manuel de Lardizabal 4, E-20018 San Sebastian, Spain^{**}*

A battery is a classical apparatus which converts a chemical reaction into a persistent voltage bias able to power electronic circuits. Similarly, a phase battery is a quantum equipment which provides a persistent phase bias to the wave function of a quantum circuit. It represents a key element for quantum technologies based on quantum coherence. Unlike the voltage batteries, a phase battery has not been implemented so far, mainly because of the natural rigidity of the quantum phase that, in typical quantum circuits, is imposed by the parity and time-reversal symmetry constrains. Here we report on the first experimental realization of a phase battery in a hybrid superconducting circuit. It consists of an n-doped InAs nanowire with unpaired-spin surface states and proximitized by Al superconducting leads. We find that the ferromagnetic polarization of the unpaired-spin states is efficiently converted into a persistent phase bias φ_0 across the wire, leading to the anomalous Josephson effect [1, 2]. By applying an external in-plane magnetic field a continuous tuning of φ_0 is achieved. This allows the charging and discharging of the quantum phase battery and reveals the symmetries of the anomalous Josephson effect predicted by our theoretical model. Our results demonstrate how the combined action of spin-orbit coupling and exchange interaction breaks the phase rigidity of the system inducing a strong coupling between charge, spin and superconducting phase. This interplay opens avenues for topological quantum

technologies [3], superconducting circuitry [4, 5] and advanced schemes of circuit quantum electrodynamics [6, 7].

At the base of phase-coherent superconducting circuits is the Josephson effect [8]: a quantum phenomenon describing the flow of a dissipationless current in weak-links between two superconductors. The Josephson current I_J is then intimately connected to the macroscopic phase difference φ between the two superconductors via the so called current-phase relationship (CPR) $I_J(\varphi)$. If either time-reversal ($t \rightarrow -t$) or inversion ($\vec{r} \rightarrow -\vec{r}$) symmetries are preserved, $I_J(\varphi)$ is an odd function of φ and the CPR, in its simplest form, reads $I_J(\varphi) = I_C \sin(\varphi)$ [9], with I_C being the junction critical current. This means that, as long as one of these symmetries is preserved, an open Josephson junction (JJ) ($I_J = 0$) cannot provide a phase bias or, accordingly, a JJ closed on a superconducting circuit ($\varphi = 0$) cannot generate current. As a consequence, the implementation of a phase battery [10] is prevented by these symmetry constraints which impose a rigidity on the superconducting phase, a universal constraint valid for any quantum phase [11, 12].

The break of time-reversal symmetry (alone) maintains the phase-rigidity but enables two possible phase shifts 0 or π in the CPR. The 0- π transition has been extensively studied in superconductor/ferromagnet/superconductor junctions [9, 13] which has applications in cryogenic memories [14, 15]. On the other hand, if both, time-reversal and inversion symmetries are broken a finite phase shift $0 < \varphi_0 < \pi$ can be induced [2, 16] and the CPR reads:

$$I_J(\varphi) = I_C \sin(\varphi + \varphi_0). \quad (1)$$

A junction with such CPR, defined as a φ_0 -junction [1], will generate a constant phase bias $\varphi = -\varphi_0$ in an open circuit configuration, while inserted into a closed superconducting loop will induce a current $I = I_C \sin(\varphi_0)$, usually denoted as *anomalous* Josephson current. Recently, anomalous Josephson currents have been the subject of theoretical [10, 17] and experimental works [18–20] envisioning direct applications on superconducting electronics and spintronics [4, 10].

Lateral hybrid junctions made of materials with a

* elia.strambini@sns.it

† andrea.iorio@sns.it

‡ fs.bergeret@csic.es

§ francesco.giazotto@sns.it

¶ IKERBASQUE, Basque Foundation for Science - E-48011 Bilbao, Spain; Donostia International Physics Center (DIPC), Manuel de Lardizabal 4, E-20018 San Sebastian, Spain

** Centro de Física de Materiales (CFM-MPC), Centro Mixto CSIC-UPV/EHU, Manuel de Lardizabal 5, E-20018 San Sebastian, Spain

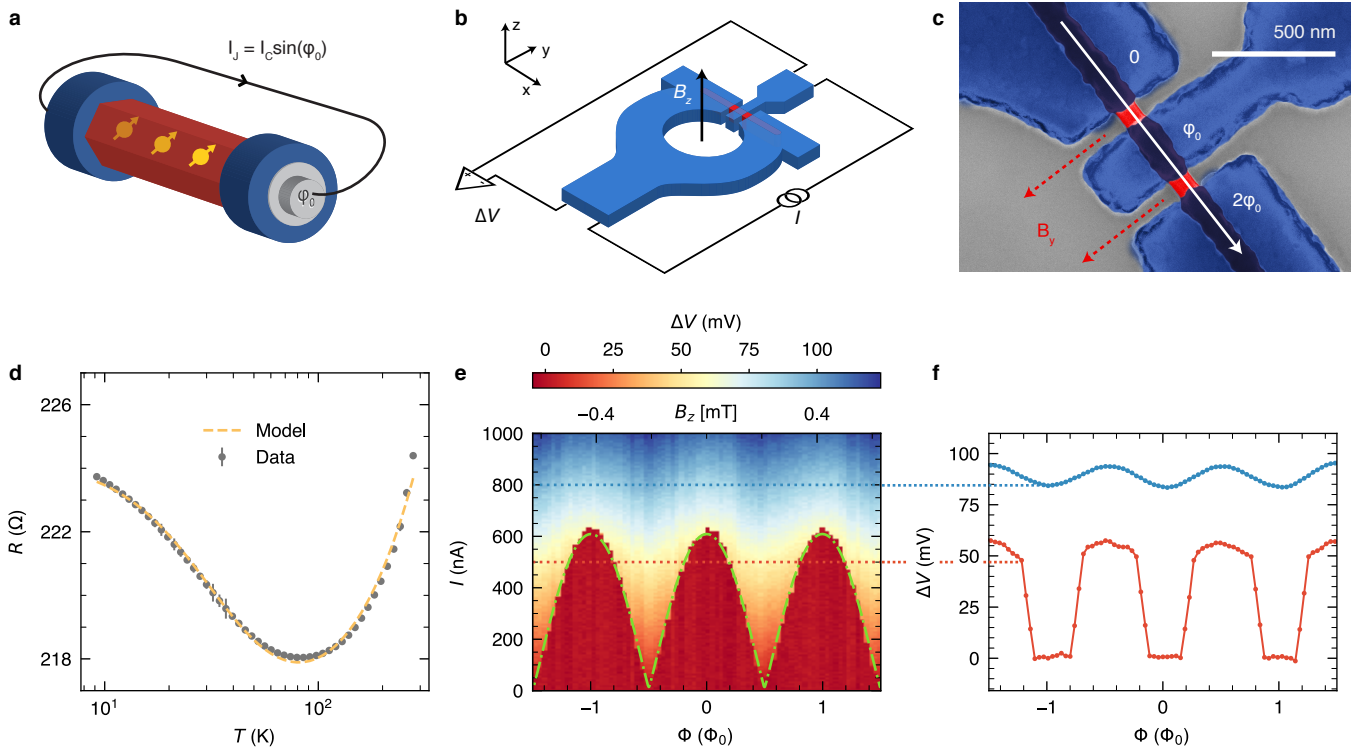


FIG. 1. Josephson phase-battery device. **a**, Conceptual scheme of a Josephson phase battery composed by an InAs nanowire (red) embedded between two superconducting poles (blue) converting the spin polarization of surface unpaired spins (yellow) into a phase bias φ_0 . The battery, inserted into a superconducting circuit, can generate a supercurrent proportional to $\sin(\varphi_0)$. **b**, Schematic illustration of the hybrid InAs nanowire-aluminum SQUID interferometer used to quantify the phase bias φ_0 provided by the two JJs (in red). The ring lies in the $x-y$ plane with the nanowire parallel to the x -axis. A magnetic field B_z piercing the ring is used to modulate the SQUID critical current (I_S) measured with a 4-wire setup. I is the current flowing through the interferometer, whereas ΔV is the resulting voltage drop across the device. **c**, False-colored SEM image of the active region of the phase battery composed by the two φ_0 -junctions. B_y is the in-plane magnetic field orthogonal to the nanowire. **d**, Temperature dependence $R(T)$ of the normal-state resistance of the interferometer showing a Kondo upturn at low temperatures which is consistent with a background of magnetic impurities. From the fit (yellow curve) we estimate a spin density of ~ 4 ppm. Error bars indicate the resistance standard deviations between two temperature points. **e**, Voltage drop ΔV measured across the SQUID versus current bias I and magnetic flux (field) $\Phi(B_z)$. The periodicity of I_S as a function of B_z translates into a periodicity on the flux $\Phi = B_z A$ through the ring with an effective area $A \simeq 4.9 \mu\text{m}^2$, consistent with the area estimated from Fig. S9 in the Supplementary Information. The green line is the best-fit of the SQUID critical current $I_S(\Phi)$ (Eq. (3)) defined by the interface between the dissipationless (red area) and the dissipative regime (coloured). **f**, Traces of $\Delta V(\Phi)$ from **e**, measured for two selected values of the current bias (below and above $2I_C$) which demonstrate the Φ_0 -periodicity both in the dissipationless and in the dissipative regime. Data in **e** and **f** were recorded at a bath temperature of 50 mK.

strong spin-orbit interaction [18, 20] or topological insulators [19] are ideal candidates to engineer Josephson φ_0 -junctions. The lateral arrangement breaks the inversion symmetry and provides a natural polar axis $\hat{\mathbf{z}}$ perpendicular to the current direction. Moreover, the electron spin polarization induced by either a Zeeman field or the exchange interaction with ordered magnetic impurities, breaks the time-reversal symmetry. In this case, the anomalous φ_0 -shifts is ruled by the Lifshitz-type invariant in the free energy (F_L), which has the form [2]:

$$F_L \sim f(\alpha, h)(\mathbf{n}_h \times \hat{\mathbf{z}}) \cdot \mathbf{v}_s, \quad (2)$$

where $f(\alpha, h)$ is an odd function of the strength of the

Rashba coefficient α and the exchange or Zeeman field h , \mathbf{n}_h is a unit vector pointing in the direction of the latter, and \mathbf{v}_s is the superfluid velocity of the Cooper pairs flowing in the JJ. The scalar triple product then defines the vectorial symmetries of φ_0 , while the amplitude of the shift depends on sample-specific microscopic details as well as macroscopic quantities like temperature.

Driven by the geometric condition for a finite φ_0 -shift (Eq. (2)), we realized a phase battery (Fig. 1a and b) consisting of a JJ made of an InAs nanowire (in red) embedded between two Al superconducting poles (in blue). The supercurrent, and hence \mathbf{v}_s , flows along the wire (x -direction) which is orthogonal to the effective $SU(2)$ Rashba magnetic field vector pointing out of the sub-

strate plane (z -direction) hosting the InAs nanowire. In the same nanowire, surface oxides or defects generate unpaired spins behaving like ferromagnetic impurities (represented by yellow arrows in Fig. 1a) that can be polarized along the y -direction to provide a persistent exchange interaction h in this direction. This leads to a finite triple product in Eq. (2) and, consequently, to the anomalous φ_0 phase bias.

An Al-based superconducting quantum interference device (SQUID) is used as a phase-sensitive interferometer made with two φ_0 -JJs (in red), as shown in Fig. 1b, c (see Section I of the Supplementary Information for fabrication detail). The device geometry has been conceived to maximize the symmetry of the two JJs [21] to accumulate the two anomalous φ_0 -shifts when applying a uniform in-plane magnetic field. The anomalous phase shift in the SQUID critical current, is then given by:

$$I_S(\Phi) = 2I_C \left| \cos \left(\pi \frac{\Phi}{\Phi_0} + \frac{\varphi_{tot}}{2} \right) \right|, \quad (3)$$

where I_C is the critical current of each JJ, Φ is the magnetic flux piercing the ring, $\varphi_{tot} = 2\varphi_0$ is the total anomalous phase shift in the SQUID interference pattern resulting from the φ_0 -shifts in each JJs (see Section IV of the Supplementary Information for details), and $\Phi_0 = 2.067 \times 10^{-15}$ Wb is the flux quantum. This model provides a good description of the SQUID interference pattern displayed in Fig. 1e, which shows the voltage drop across the SQUID as a function of the out-of-plane magnetic field B_z and bias current I . The red-colored region of Fig. 1e, corresponding to zero-voltage drop, indicates the dissipationless superconducting regime and the edge of this region provides the $I_S(\Phi)$ dependence. The green line on top of the color plot is the best-fit of $I_S(\Phi)$ from Eq. (3), with $I_c \simeq 300$ nA and no phase-shift $\varphi_{tot} \simeq 0$. The latter condition is consistent with the absence of the anomalous phase when the magnetic field has only a component in $\hat{\mathbf{z}}$ direction and the magnetic impurities are not polarized (i.e. $\mathbf{n}_h \parallel \hat{\mathbf{z}}$ in Eq. (2)). Notably, there is a replica of the $I_S(\Phi)$ oscillations in the voltage drop $\Delta V(\Phi)$ when $I > I_S$, and the SQUID operates in the dissipative regime (blue region and curve in Figs. 1e-f), as conventionally realized with strongly overdamped JJs [22]. This oscillation provides a complementary and fast method to quantify the SQUID phase shifts and is used in the following analysis. Additional measurements on similar devices can be found in Section VII of the Supplementary Information.

The temperature dependence of the device normal-state resistance shows an upturn below ~ 80 K (see Fig. 1d) which is a clear signature of the presence of magnetic impurities that increase, at low temperature, the electron scattering events. The upturn can be well fitted by the Kondo model (yellow line of Fig. 1d) for spin 1/2 of magnetic impurities with a density of ~ 4 ppm (see Section II of the Supplementary Information for more details on the fitting procedure). The presence of these unpaired spins can be ascribed to the nanowire surface ox-

ides, as already observed in undoped metal oxide nanostructures [23], even if defects in the nanowire crystalline structure [24] cannot be excluded a priori. Although, the amount of intrinsic magnetic impurities is not fully controllable, their presence is crucial for the operation and implementation of the phase battery, as discussed below.

Following the condition imposed by a finite Lifshitz invariant term (Eq. (2)) we apply an in-plane magnetic field orthogonal to the nanowire axis (B_y) to maximize the effect. The $I_S(\Phi)$ dependence then evolves with a clear generation of an anomalous phase shift, as presented in the panels of Fig. 2. The evolution of $\Delta V(\Phi)$ as a function of B_y ranging from -60 mT up to 60 mT is visible in Fig. 2a and in the selected single traces of Fig. 2b. The resulting phase-shift, φ_{tot} exhibits a non-monotonic evolution as a function of B_y , with a maximum shift at $B_y \simeq 5$ mT and a saturation for $|B_y| \gtrsim 30$ mT (yellow curve in Fig. 2c). When the field is reversed, a hysteretic behavior is observed (green curve in Fig. 2c), and the evolution of φ_{tot} reverses with a minimum shift at $B_y \simeq -5$ mT. The change of sign of the phase-shift agrees with the theoretical prediction of Eq. (2) when $\mathbf{h} \rightarrow -\mathbf{h}$, whereas the observed hysteretic behavior suggests a ferromagnetic coupling between the magnetic impurities in the nanowire. Trivial hysteretic phase shifts induced by a trapped flux in the superconductor [25] or in the SQUID ring can be excluded (see Section VI of the Supplementary Information for more details). At low temperatures, the coexistence of Kondo and ferromagnetism is not unusual [23] and well describes the hysteretic non-monotonic behavior observed in $\varphi_{tot}(B_y)$. Indeed, due to the antiferromagnetic nature of the Kondo interaction, the effective exchange field created by these unpaired spins is opposite to the Zeeman field generated by B_y so that the two contributions are competing in the anomalous phase with a partial cancellation.

This additional component is confirmed by the observation of an *intrinsic* phase-shift, φ_{int} , which is present even in the absence of the in-plane magnetic field ($B_y = 0$) if a finite B_y has been previously applied, as shown in Figs. 2d and e. Since it stems from a ferromagnetic ordering, φ_{int} depends only on the history of B_y , and again, the evolution of $\varphi_{int}(B_y)$ can be extracted and is presented in Fig. 2f. In contrast to the total phase-shift, φ_{int} follows a clear and almost monotonic behavior which shows a hysteresis in the back and forth sweep direction (blue and red curves of Fig. 2f). φ_{int} saturates at $|B_y| \gtrsim 15$ mT in the two asymptotic limits with total phase drop of $\sim \pi$. Furthermore, during the first magnetization of the SQUID, a clear curve resembling the initial magnetization curve of a ferromagnet has been observed (see Fig. S2 in the Supplementary Information), confirming the ferromagnetic nature of the impurity ensemble.

We now analyze the *extrinsic* contribution, φ_{ex} , to the phase shift which stems directly from the external B -field. Due to the additive nature of the anomalous phase in the exchange field, h in Eq. (2), it is possible to extract from φ_{tot} the extrinsic contribution $\varphi_{ex} = \varphi_{tot} - \varphi_{int}$.

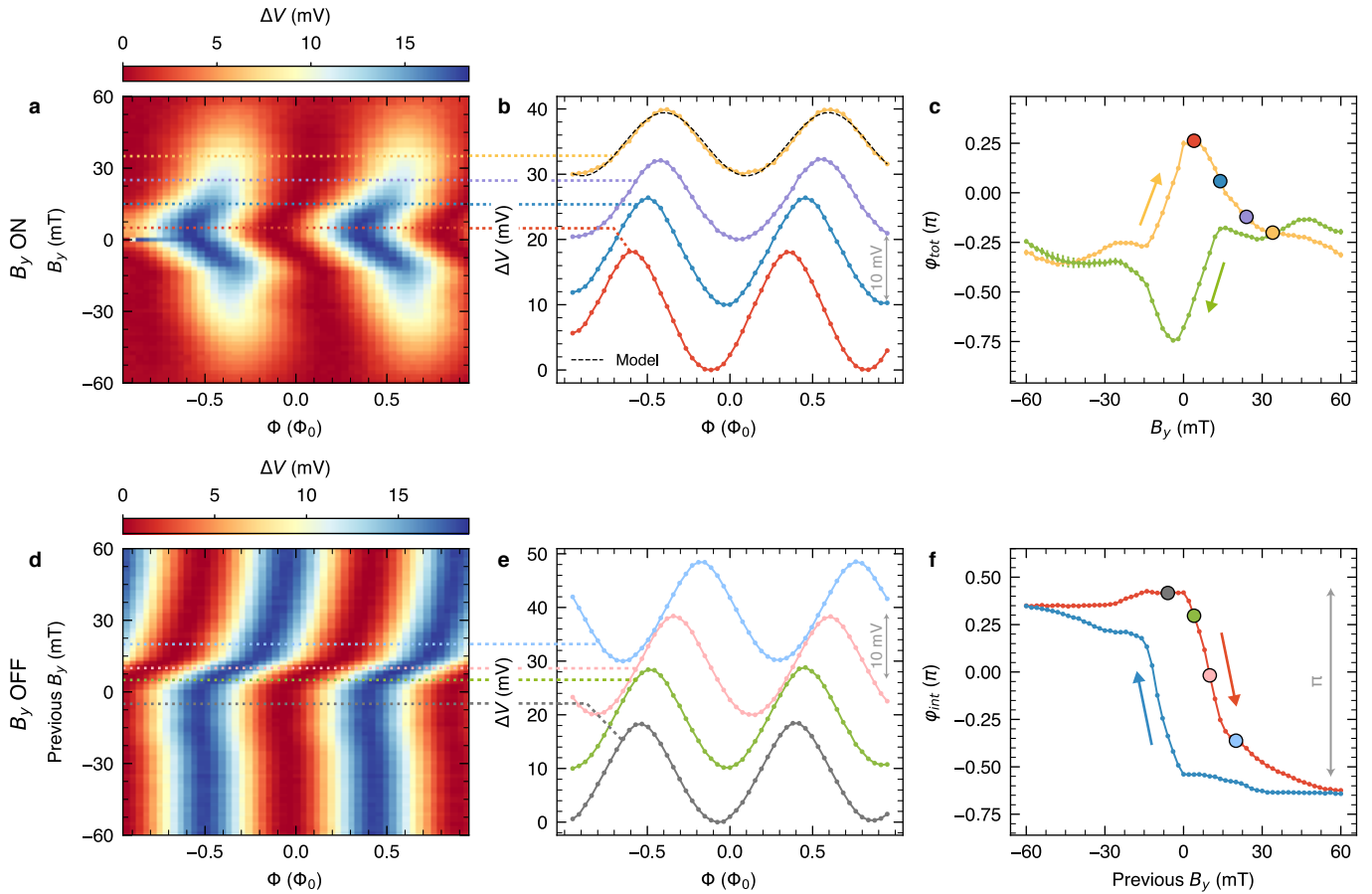


FIG. 2. **Charging loops of the Josephson phase battery.** **a**, Voltage drop $\Delta V(\Phi)$ at constant current bias $I = 1 \mu\text{A}$ versus in-plane magnetic field B_y applied orthogonal to the nanowire axis. At large $|B_y|$, the amplitude of $\Delta V(\Phi)$ is lowered due to the suppression of superconductivity inside the wire. Each trace is vertically offset for clarity. **b**, Selected traces $\Delta V(\Phi)$ extracted from **a** for different B_y . Data are vertically offset for clarity. **c**, Extracted phase shift φ_{tot} from the curves in **a** with back (green) and forth (yellow) sweeps in B_y . The shifts are extracted by comparing the single traces to the RSJ relation $\Delta V = \frac{R}{2} \sqrt{I^2 - 4I_C^2 \cos(\pi\Phi/\Phi_0 + \varphi_{tot}/2)^2}$ [22], see the dashed line in **b** which serves as an example. **d**, Color plot of the persistent voltage drop $\Delta V(\Phi)$ measured at $B_y = 0$ after the magnetic field was swept to the values shown on the y -axis. **e**, Selected traces $\Delta V(\Phi)$ extracted from **d**. **f**, Intrinsic phase shift φ_{int} extracted from **d**. φ_{int} stems from the ferromagnetic polarization of the unpaired spins. Error bars in **c** and **f** indicate the 1σ standard errors resulting from the fit of the curves in **b** and **e**. All data were recorded at 50 mK of bath temperature.

This is depicted in Fig. 3a, where the evolution of φ_{ex} in B_y is shown. Here, the agreement between the back (blue) and forth (red) traces in B_y demonstrates implicitly the absence of any hysteresis ensuring the complete extraction of the intrinsic contribution. Notice also that the behavior of φ_{int} and φ_{ex} in the magnetic field is *opposite* in sign as expected from the competition between the exchange interactions induced by the Kondo anti-ferromagnetic coupling and a Zeeman field, then further supporting our assumptions. The dependence $\varphi_{ex}(B_y)$ is characterized by a linear increase at low magnetic fields ($|B_y| < 15 \text{ mT}$) up to a maximum phase-shift of $\pm\pi/2$. Remarkably, our measurement reveals the *odd* parity of the anomalous phase with respect to the magnetic field, one of the main symmetry hallmarks of this effect [1, 2]. This parity is the consequence of the odd

parity of the free energy F_L with respect to the exchange field. At higher fields non-linearities appear suggesting a non-trivial evolution of φ_{ex} in the magnetic field. In order to understand this behavior we have modelled our φ_0 -junction setup by a lateral junction treated within the quasi-classical approach presented in Ref. [2] (see Section V in the Supplementary Information). The resulting φ_0 obtained from the above model, is shown in the inset of Fig. 3a. It nicely reproduces the main features of φ_{ex} : the linear dependence at small magnetic fields and the saturation at larger ones. Notice that, within the scale of the magnetic field applied in the experiment, the field dependence of the anomalous phase looks as it saturates at the value close to $\pi/2$. This value is however non-universal and depends on the characteristics of the nanowire. Moreover, if larger values of B_{in} could be

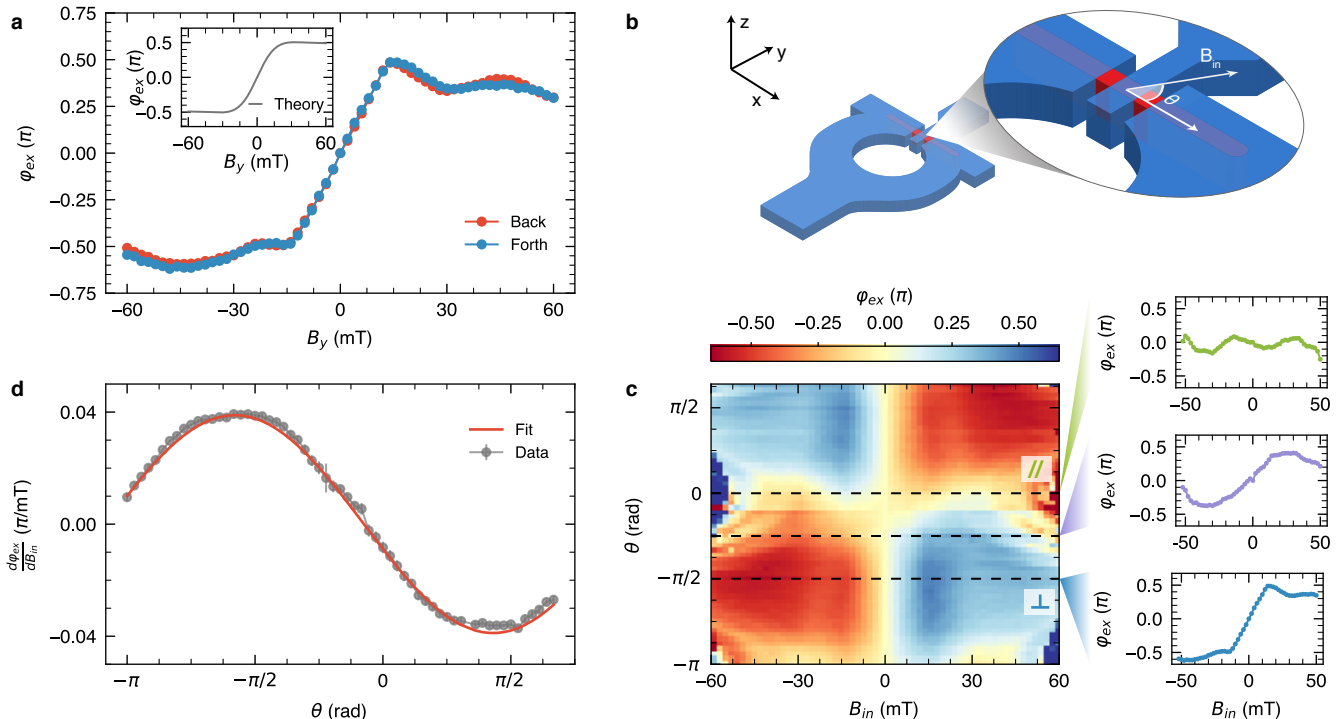


FIG. 3. **Vectorial symmetry of the anomalous phase** φ_0 . **a**, Dependence of the extrinsic anomalous phase φ_{ex} on B_y . It results in an odd symmetry and non-hysteretic back and forth sweeps (blue and red traces). Inset: The $\varphi_{ex}(B_y)$ dependence obtained from the theoretical model (see Section V of the Supplementary Information for details). **b**, Sketch of the interferometer with the reference axes of the in-plane magnetic field (B_{in}) and the angle θ with respect to the nanowire axis. **c**, Dependence of the anomalous phase φ_{ex} on θ and B_{in} . The single traces on the right show the behavior of φ_{ex} for a longitudinal $\theta = 0$ (green curve), canted $\theta = \pi/4$ (violet curve) and orthogonal field $\theta = \pi/2$ (blue curve). **d**, $d\varphi_{ex}/dB_{in}$ versus θ together with a sinusoidal fit (red curve) from Eq. (4). The slope has been evaluated by a linear fit of the data in **b** for $|B_{in}| < 10$ mT. The error bar is the 1σ standard error of the fit. All the data were recorded at 50 mK of bath temperature.

reached, the anomalous phase of each junction would increase up to the universal plateau at π , as expected also for planar junctions [2].

At small in-plane fields ($B_{in} = \sqrt{B_x^2 + B_y^2}$) the model leads to a simple expression for the anomalous phase:

$$\varphi_{ex} \simeq C_1 \alpha^3 B_{in} \sin(\theta) + O(B_{in}^3), \quad (4)$$

where θ is the angle between the field and the nanowire axis, C_1 is a parameter dependent on the temperature and the microscopic details of the JJ and O is the polynomial asymptotic notation. By using typical values of the parameters for the InAs/Al junction we obtained a $C_1 \approx 0.04 \pi/\text{mT}$, in very good agreement with the experimental data (see Section V in the Supplementary Information).

The odd symmetry of the anomalous phase dictated by the triple product in Eq. (2) can be further investigated by measuring φ_{ex} over all the directions of the in-plane magnetic field. Figure 3c shows the full dependence of φ_{ex} on the angle θ (see sketch in Fig. 3b). As predicted from Eq. (2), the phase-shift is very small for fields along the nanowire axis ($\theta = 0$, green trace in Fig. 3c), showing the maximum slope for the orthogonal magnetic field

($\theta = \pi/2$, blue trace in Fig. 3c). The odd symmetry manifests clearly as well in the slope $\frac{\partial \varphi_{ex}}{\partial B_{in}}$ in the low-field limit (Fig. 3d). The latter is perfectly fitted with a sinusoidal function of θ in agreement with Eq. (4) (red trace in Fig. 3d).

In summary, our results demonstrate the implementation of a quantum phase battery. This quantum element, providing a controllable and localized phase-bias, can find key applications in different quantum circuits such as energy tuner for superconducting flux [26] and hybrid [27] qubits, or persistent multi-valued phase-shifter for superconducting quantum memories [15, 28] as well as superconducting rectifiers [29]. Moreover, the magnetic control over the superconducting phase opens new avenues for advanced schemes of topological superconducting electronics [30] based on InAs JJs [18, 31]. The weak control over the density of unpaired spins makes our proof-of-concept device difficult to reproduce in a massive reliable process. Further technological improvements can be envisioned by a controlled doping of the wires with magnetic impurities [32] or by the inclusion of a thin epitaxial layer of a ferromagnetic insulator, like EuS [33], as recently integrated in similar nanowires [34].

ACKNOWLEDGEMENT

The work of E.S. was supported by a Marie Curie Individual Fellowship (MSCA-IFEF-ST No.660532-SuperMag). E.S., N.L and F.G acknowledge partial financial support from the European Union’s Seventh Framework Programme (FP7/2007-2013)/ERC Grant No. 615187- COMANCHE. E.S., A.I., O.D., N.L, F.S.B. and F.G were partially supported by EU’s Horizon 2020 research and innovation program under Grant Agreement No. 800923 (SUPERTED). L.S and V. Z. acknowledge partial support by the SuperTop QuantERA network and the FET Open And QC. I.V.T, C.S.F., and F.S.B., acknowledge financial support by the Spanish Ministerio de Ciencia, Innovacion y Universidades through the Projects No. FIS2014-55987-P, FIS2016-79464-P and No. FIS2017-82804-P and by the grant “Grupos Consolidados UPV/EHU del Gobierno Vasco” (Grant No. IT1249-19). A.B. acknowledges the CNR-CONICET cooperation

program “Energy conversion in quantum nanoscale hybrid devices,” the SNS-WIS joint laboratory QUANTRA, funded by the Italian Ministry of Foreign Affairs and International Cooperation and the Royal Society through the international exchanges between the United Kingdom and Italy (Grant No. IEC R2192166).

AUTHOR CONTRIBUTION

E.S. A.I. and O.D. performed the experiment and analyzed the data. R.C.,C.S.F.,C.G.,I.V.T., A.B. and F.S.B. provided theoretical support. M.R., N.L. and O.D. fabricated the phase battery on the InAs nanowires grown by V.Z. and L.S.. E.S. conceived the experiment together with F.G. that supervised the project. E.S., A.I., I.V.T. and F.S.B. wrote the manuscript with feedback from all authors.

-
- [1] Buzdin, A. Direct coupling between magnetism and superconducting current in the josephson φ_0 junction. *Phys. Rev. Lett.* **101**, 107005 (2008).
- [2] Bergeret, F. S. & Tokatly, I. V. Theory of diffusive φ_0 Josephson junctions in the presence of spin-orbit coupling. *EPL* **110**, 57005 (2015).
- [3] Alicea, J. Exotic matter: Majorana modes materialize. *Nat Nano* **8**, 623–624 (2013).
- [4] Linder, J. & Robinson, J. W. A. Superconducting spintronics. *Nat Phys* **11**, 307–315 (2015).
- [5] Fornieri, A. & Giazotto, F. Towards phase-coherent caloritronics in superconducting circuits. *Nature Nanotech* **12**, 944–952 (2017).
- [6] Wallraff, A. *et al.* Strong coupling of a single photon to a superconducting qubit using circuit quantum electrodynamics. *Nature* **431**, 162–167 (2004).
- [7] Chiorescu, I. *et al.* Coherent dynamics of a flux qubit coupled to a harmonic oscillator. *Nature* **431**, 159–162 (2004).
- [8] Josephson, B. D. Possible new effects in superconductive tunnelling. *Physics Letters* **1**, 251–253 (1962).
- [9] Golubov, A. A., Kupriyanov, M. Y. & Il’ichev, E. The current-phase relation in Josephson junctions. *Rev. Mod. Phys.* **76**, 411–469 (2004).
- [10] Pal, S. & Benjamin, C. Quantized Josephson phase battery. *EPL* **126**, 57002 (2019).
- [11] Yacoby, A., Schuster, R. & Heiblum, M. Phase rigidity and $h/2e$ oscillations in a single-ring Aharonov-Bohm experiment. *Phys. Rev. B* **53**, 9583–9586 (1996).
- [12] Strambini, E., Piazza, V., Biasiol, G., Sorba, L. & Beltram, F. Impact of classical forces and decoherence in multiterminal Aharonov-Bohm networks. *Phys. Rev. B* **79**, 195443 (2009).
- [13] Ryazanov, V. V. *et al.* Coupling of Two Superconductors through a Ferromagnet: Evidence for a π Junction. *Phys. Rev. Lett.* **86**, 2427–2430 (2001).
- [14] Baek, B., Rippard, W. H., Benz, S. P., Russek, S. E. & Dresselhaus, P. D. Hybrid superconducting-magnetic memory device using competing order parameters. *Nature Communications* **5**, 3888 (2014).
- [15] Gingrich, E. C. *et al.* Controllable $0-\pi$ Josephson junctions containing a ferromagnetic spin valve. *Nat Phys* **12**, 564–567 (2016).
- [16] Silaev, M., Tokatly, I. & Bergeret, F. Anomalous current in diffusive ferromagnetic josephson junctions. *Physical Review B* **95**, 184508 (2017).
- [17] Yokoyama, T. & Nazarov, Y. V. Magnetic anisotropy of critical current in nanowire Josephson junction with spin-orbit interaction. *EPL* **108**, 47009 (2014).
- [18] Szombati, D. B. *et al.* Josephson φ_0 -junction in nanowire quantum dots. *Nat Phys* **12**, 568–572 (2016).
- [19] Assouline, A. *et al.* Spin-orbit induced phase-shift in Bi_2Se_3 Josephson junctions. *Nature Communications* **10**, 126 (2019).
- [20] Mayer, W. *et al.* Gate controlled anomalous phase shift in Al/InAs Josephson junctions. *Nat Commun* **11**, 1–6 (2020).
- [21] Giazotto, F. *et al.* A Josephson quantum electron pump. *Nat. Phys.* **7**, 857–861 (2011).
- [22] Clarke, J. & Braginski, A. I. (eds.) *The SQUID handbook* (Wiley-VCH, Weinheim, 2004).
- [23] Sapkota, K. R., Maloney, F. S. & Wang, W. Observations of the Kondo effect and its coexistence with ferromagnetism in a magnetically undoped metal oxide nanostructure. *Phys. Rev. B* **97**, 144425 (2018).
- [24] Dietl, T. & Ohno, H. Engineering magnetism in semiconductors. *Materials Today* **9**, 18–26 (2006).
- [25] Golod, T., Rydh, A. & Krasnov, V. M. Detection of the phase shift from a single abrikosov vortex. *Phys. Rev. Lett.* **104**, 227003 (2010).
- [26] Pita-Vidal, M. *et al.* A gate-tunable, field-compatible fluxonium. *arXiv:1910.07978 [cond-mat, physics:quant-ph]* (2019).
- [27] Larsen, T. *et al.* Semiconductor-Nanowire-Based Superconducting Qubit. *Phys. Rev. Lett.* **115**, 127001 (2015).

- [28] Guarcello, C. & Bergeret, F. Cryogenic Memory Element Based on an Anomalous Josephson Junction. *Phys. Rev. Applied* **13**, 034012 (2020).
- [29] Reynoso, A. A., Usaj, G., Balseiro, C. A., Feinberg, D. & Avignon, M. Spin-orbit-induced chirality of Andreev states in Josephson junctions. *Phys. Rev. B* **86**, 214519 (2012).
- [30] Virtanen, P., Bergeret, F. S., Strambini, E., Giazotto, F. & Braggio, A. Majorana bound states in hybrid two-dimensional Josephson junctions with ferromagnetic insulators. *Phys. Rev. B* **98**, 020501 (2018).
- [31] Tiira, J. *et al.* Magnetically-driven colossal supercurrent enhancement in InAs nanowire Josephson junctions. *Nature Communications* **8**, 14984 (2017).
- [32] Martelli, F. *et al.* Manganese-Induced Growth of GaAs Nanowires. *Nano Lett.* **6**, 2130–2134 (2006).
- [33] Strambini, E. *et al.* Revealing the magnetic proximity effect in EuS/Al bilayers through superconducting tunneling spectroscopy. *Phys. Rev. Materials* **1**, 054402 (2017).
- [34] Liu, Y. *et al.* Semiconductor–Ferromagnetic Insulator–Superconductor Nanowires: Stray Field and Exchange Field. *Nano Lett.* **20**, 456–462 (2020).

Supplementary Information

I. DEVICE FABRICATION

Hybrid proximity DC SQUIDS devices were fabricated starting from gold catalyzed n -doped InAs nanowires with typical length of $1.5\ \mu\text{m}$ and a diameter of $\sim 85\ \text{nm}$ grown by chemical beam epitaxy [1]. The n -doping was obtained with Se [2] and the metalorganic precursors for the nanowire growth was trimethylindium (TMIn), tertiarybutylarsine (TBAs) and ditertiarybutylselenide (DTSe), with line pressures of 0.6, 1.5 and 0.3 Torr respectively. Nanowires were drop-casted onto a substrate consisting of 300 nm thick SiO_2 on p -doped Si. Afterwards, a 280 nm-thick layer of positive-tone Poly(methyl methacrylate) (PMMA) electron beam resist was spun onto the substrate. The devices were then manually aligned to the randomly distributed InAs nanowires and patterned by means of standard electron beam lithography (EBL) followed by electron beam evaporation (EBE) of superconducting Ti/Al (5/100 nm) electrodes. Low-resistance ohmic contacts between the superconducting leads and the InAs nanowires were promoted by exposing the InAs nanowire contact areas to a highly diluted ammonium polysulfide $(\text{NH}_4)_2\text{S}_x$ solution, which selectively removes the InAs native oxide and passivates the surface, prior to EBE. The fabrication process was finalized by dissolving the PMMA layer in acetone.

From transport characterization on similar wires and normal metal electrodes [3], we estimate a typical electron concentration $n \simeq 2 \times 10^{18}\ \text{cm}^{-3}$ and mobility $\mu \simeq 1200\ \text{cm}^2/\text{Vs}$. The corresponding Fermi velocity v_F , mean free path l_e and diffusion coefficient $D = v_F l_e / 3$, are evaluated to be $v_F \simeq 2 \times 10^6\ \text{m/s}$, $l_e \simeq 30\ \text{nm}$ and $D \simeq 200\ \text{cm}^2/\text{s}$.

II. KONDO RESISTANCE $R(T)$

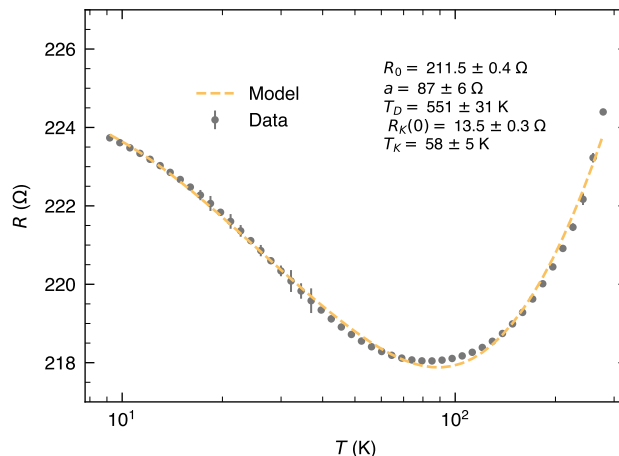


FIG. S1. **Kondo upturn of the InAs nanowire.** Resistance versus temperature $R(T)$ of one of the devices measured during the cooldown of the refrigerator showing a clear increase of resistance for temperature below 80 K. This behaviour is consistent with the Kondo scattering model as demonstrated by the good fit of the $R - T$ data with the model in Eq. S3.

To quantify the amount of unpaired spins in our system the temperature dependence of the normal-state resistance $R(T)$ has been studied in the range 10 K to 300 K. The data exhibits an upturn at $T \sim 80\ \text{K}$ (see Fig. S1) suggesting a Kondo scattering mechanisms between the free electrons and the unpaired spins in the weak-links. Since the InAs nanowires were synthesized without incorporating any magnetic impurity (to the best of our knowledge, Se doping cannot provide by itself any magnetism), we conjecture that unpaired spins are originated from oxides states at the nanowire surface, in analogy with what is observed in metallic nanowires [4, 23]. Indeed, the $R(T)$ of a diluted magnetic alloy follows the universal non-monotonic relation [6]

$$R(T) = R_0 + R_{el-ph}(T) + R_K(T), \quad (\text{S1})$$

where R_0 is the residual resistance while $R_{el-ph}(T)$ and $R_K(T)$ are the contribution given respectively by the electron-phonon and the Kondo scattering. The temperature dependence of the former can be expressed according to the

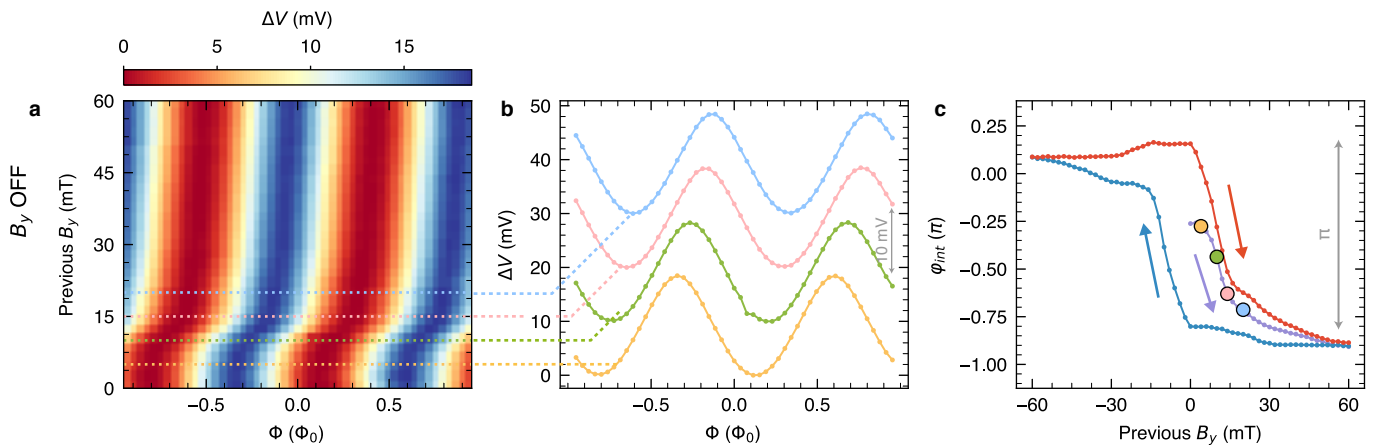


FIG. S2. **First magnetization curve of φ_{int} .** **a**, Color plot of the voltage drop $\Delta V(\Phi)$ measured at $B_y = 0$ after the magnetic field was swept to the values shown on the y -axis straight after the thermal cycle. **b**, Selected traces $\Delta V(\Phi)$ corresponding to the cuts in **a**. **c**, Intrinsic phase shift φ_{int} extracted from **b**, showing the first polarization of the unpaired spins (violet curve) and the hysteresis loop followed in the subsequent back and forth sweeps of B_y , blue and red curves, respectively.

Bloch-Gruneisen model as [7]

$$R_{el-ph}(T) = a \left(\frac{T}{\theta_D} \right)^5 \int_0^{\theta_D/T} \frac{x^5}{(e^x - 1)(1 - e^{-x})} dx. \quad (S2)$$

For the Kondo contribution many analytical approximations are available according to the range of temperature investigated. In the full range of temperature the exact solution exist from the numerical renormalization group theory (NRG). In the following we use an empirical fitting function derived as an analytical approximation of the NRG given by [8–11]

$$R_K^{NRG} = R_K(0) \left(\frac{T_K'^2}{T^2 + T_K'^2} \right)^s, \quad (S3)$$

with T_K' related to the actual Kondo temperature T_K by $T_K' = T_K / (2^{1/s} - 1)^{1/2}$. Note that Eq. S3 is defined such that $R_K(T_K) = R_K(0)/2$ and the parameter s is fixed to $s = 0.22$ as expected for a spin 1/2 impurity. In Fig. S1 we show the fit of the experimental data with Eq. S3, from which we extract a Kondo temperature $T_K = 58 \pm 5$ K, a residual magnetic impurity resistance $R_K(0) = 13.5 \pm 0.3 \Omega$, a coefficient $a = 87 \pm 6 \Omega$ and a Debye temperature $\theta_D = 551 \pm 31$ K. From $R_K(0)$ is possible to estimate the density of unpaired spin, that form the Hamann expression of the residual Kondo resistance in the unitary limit is given by [12]

$$R_K(0) = \frac{L}{A} \frac{4\pi\hbar}{nk_F e^2}, \quad (S4)$$

with $L \sim 80$ nm junction lengths, $A \sim \pi r^2$ with $r \sim 45$ nm nanowire cross-sectional area, k_F Fermi wavevector and n electron carrier density, from which we estimate the density of magnetic impurities $c \simeq 1.36 \times 10^{17} \text{ cm}^{-3}$. This corresponds to a concentration of ~ 4 ppm ($= c/n_{InAs}$, with the InAs atomic density $n_{InAs} = 3.59 \times 10^{22} \text{ cm}^{-3}$) of unpaired spins in the InAs nanowire.

III. FIRST “MAGNETIZATION” CURVE

The persistent hysteretic loops of the φ_0 -shift, shown in Fig. 1d-f of the main text, are consistent with the presence of a ferromagnetic background of unpaired spin. To support this hypothesis, we show in Fig. S2a and b the first magnetization curve of this spin ensemble measured in the same device. Initially, the magnetization of the sample is lifted by warming the system above 3 K. Then, the SQUID voltage drop $\Delta V(\Phi)$ is measured in the absence of the in-plane magnetic field B_y which is gradually turned on thus polarizing the unpaired spins. The resulting $\Delta V(\Phi)$ shows no shifts at low B_y while, only above 5 mT a clear shift is generated. The resulting φ_{int} extracted by fitting $\Delta V(\Phi)$ is shown in the violet curve of Fig. S2c. By reversing B_y the φ_{int} then evolves with the typical hysteretic curve of a ferromagnetic system (blue and red curves in Fig. S2c).

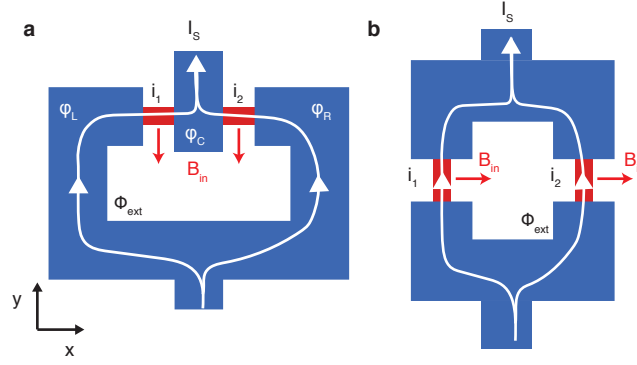


FIG. S3. **Comparison between SQUID geometries.** The SQUID geometry employed in this work **a** allows a simple readout of the anomalous phase φ_{tot} generated by a uniform magnetic field B_{in} since the opposite direction of the supercurrents in the two JJs. This would not be possible in a conventional geometry as the one shown in **b**.

IV. SQUID WITH ANOMALOUS JOSEPHSON JUNCTIONS

The critical current of a SQUID interferometer can be evaluated from the CPR of the two JJs forming the interferometer. Using a sinusoidal CPR, the currents through the two junctions can be written as

$$i_1 = I_c \sin \left[(\varphi_C - \varphi_L) + \varphi_0^{(1)} \right] \quad i_2 = I_c \sin \left[(\varphi_C - \varphi_R) + \varphi_0^{(2)} \right], \quad (S5)$$

where $\varphi_L, \varphi_C, \varphi_R$ are the left, central and right superconducting phases and I_c is the critical current of each JJ.

The supercurrent of the SQUID is the sum of the two contributions ($I_s = i_1 + i_2$), and, with the constraint on the superconducting phases of the flux quantization

$$(\varphi_L - \varphi_C) + (\varphi_C - \varphi_R) + 2\pi \frac{\Phi}{\Phi_0} = 2\pi \pmod{n}, \quad (S6)$$

it has the form

$$I_s = 2I_c \sin(\delta_0) \cos \left[\frac{1}{2} \left(2\pi \frac{\Phi}{\Phi_0} + \varphi_{tot} \right) \right], \quad (S7)$$

where $\delta_0 = \varphi_C - \frac{\varphi_L + \varphi_R}{2} + \frac{(\varphi_0^{(2)} + \varphi_0^{(1)})}{2}$ and $\varphi_{tot} = \varphi_0^{(2)} - \varphi_0^{(1)}$ is the total anomalous phase built in the interferometer. With the geometry depicted in Fig. S3a, the two junctions experience the same in-plane magnetic field orientation but the supercurrents flow in opposite directions resulting in $\varphi_0^{(1)} = -\varphi_0^{(2)} = \varphi_0$ and $\varphi_{tot} = 2\varphi_0$. The stable state configuration of the SQUID is achieved by minimizing the total Josephson free energy obtained at $\delta_0 = \pi/2$, and then the maximum sustainable supercurrent results to be

$$I_S(\Phi) = 2I_c \left| \cos \left(\pi \frac{\Phi}{\Phi_0} + \frac{\varphi_{tot}}{2} \right) \right|. \quad (S8)$$

It follows that in absence of magnetic flux, the maximum supercurrent is reduced by a factor $\sim |\cos(\varphi_{tot}/2)|$ compared to the non-anomalous case as a consequence of the anomalous supercurrent already present in the interferometer. In a more conventional geometry as the one showed in Fig. S3b, the anomalous phases acquired by the two junctions would be the same $\varphi_0^{(1)} = \varphi_0^{(2)} = \varphi_0$, making impossible its detection in the phase-to-current readout employed in the present work.

V. LATERAL φ_0 -JUNCTION

The origin of the anomalous phase φ_0 is the singlet-triplet conversion mediated by the spin-orbit coupling (SOC), which in the normal state corresponds to the charge-spin conversion [2]. The calculations of the anomalous Josephson current in φ_0 -junctions have been done for ideal planar S-N-S junctions, in which the superconducting electrodes and the normal region with SOC are separated by sharp boundaries [1, 2, 14], where the singlet-triplet coupling takes

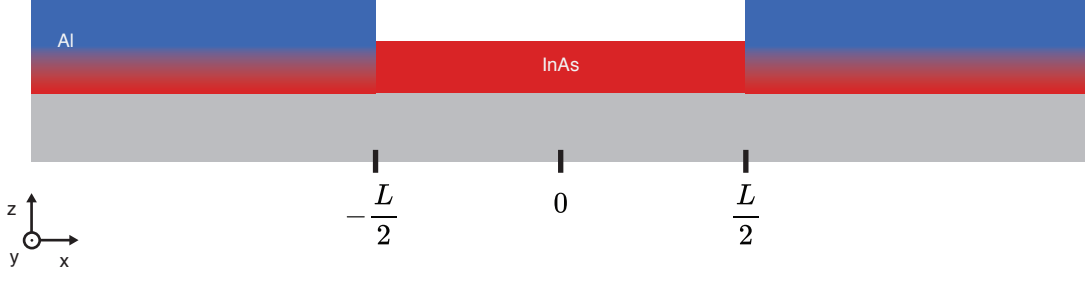


FIG. S4. **Schematic view of the S-N-S junctions.** At $|x| > L/2$, the InAs nanowire (red region) is partially covered by the Al superconducting leads (dark blue regions). The gray region corresponds to the substrate. This schematic view corresponds to the z - x plane of Fig. 3b (top panel) in the main text.

place only at N region. As shown in Ref. [2], this assumption leads to a monotonically increase of the anomalous phase φ_0 as a function of the applied magnetic field, which contrasts with curves extracted from our experiment (see Fig. 3a in the main text). It is however clear that our experimental setup (Fig. 1 in the main text) differs from an ideal S-N-S junction. Indeed, in each junction, the superconducting leads are covering part of the wires over distances larger than the coherence length. This means that the SOC, and hence the spin-charge conversion, is also finite in the portion of the wire covered by the superconductor. As we show in this section, this feature is essential to understand the experimental findings; in particular, the dependence to φ_0 from the external magnetic field. In this calculation, we focus on the dependence of φ_0 on the y direction of the field, i.e., B_{in} at $\theta = \pi/2$ (see Figs. 3a and b in the main text).

To be specific, we consider the junction sketched in Fig. S4. We assume an infinite diffusive quasi-one dimensional nanowire along the x -axis, which is partially covered by two semi-infinite Al superconducting leads at $x < L/2$ and $x > L/2$. We assume, for simplicity, that the proximity effect is weak and that the wire is diffusive. In such a case, the condensate function, which determines the Josephson current, obeys the linearized Usadel equation, which results in two coupled differential equations for the singlet and triplet components as shown in Ref. [2]. Because the wire lies on a substrate plane, the system has an uniaxial asymmetry in the z direction perpendicular to the substrate (see Fig. S4). In the presence of SOC, this allows for a gradient singlet-triplet coupling generated by a differential operator of the form $C_k^a \partial_k \sim (\hat{z} \times \nabla)^a$, which converts a scalar (the singlet) into a pseudovector (the triplet) and vice-versa [2, 14]. We consider the case when the external field is applied in the y direction, and hence, the superconducting condensate function has the form $f = f_s + i f_t \text{sgn} \omega \sigma^y$, where $f_{s,t}$ are the singlet and triplet components and ω the Matsubara frequency. The linearized Usadel equation reads:

$$\begin{aligned} \frac{D}{2} \nabla^2 f_s - |\omega| f_s + (h - iD\kappa_{sc}\partial_x) f_t &= 0, \\ \frac{D}{2} \nabla^2 f_t - |\omega| f_t - (h - 2iD\kappa_{sc}\partial_x) f_s &= 0. \end{aligned} \quad (\text{S9})$$

Here D is the diffusion coefficient and $h = \mu_B g_s B_{in}/2$ is the Zeeman field. The last term in both equations describes the spin-charge conversion due to the SOC. It is proportional to the effective inverse length κ_{sc} and the spatial variation of the condensate in the direction of the wire axis. The form of this term is determined by the uniaxial anisotropy of the setup in combination with the fact that we assume that the field is applied only in y direction.

Equation (S9) is written for the full 3D geometry. To obtain an effective 1D Usadel equation, we integrate Eq. (S9) over the wire cross-section and use boundary conditions imposed on the condensate function at the surface of the wire. In the part of the wire which is covered by the superconductor, the interface between the wire and the superconductor is described by the linearized Kupryianov-Lukichev boundary condition:

$$\partial_x f_s|_{\text{InAs/Al}} = \gamma f_{\text{BCS}} e^{i\phi}, \quad (\text{S10})$$

where γ is a parameter describing the InAs/Al interface, $f_{\text{BCS}} = \Delta/\sqrt{\omega^2 + \Delta^2}$ is the BCS bulk anomalous Green's function in the superconducting leads, and ϕ is the phase of the corresponding lead. In the uncovered parts of the wire, we impose a zero current flow which corresponds to $\partial_x f_{s/t}|_{\text{InAs/vac.}} = 0$. The integration of Eq. (S9) over the cross-section of the wire results in two coupled equations for the singlet and triplet components:

$$\begin{aligned} \partial_x^2 f_s - \kappa_\omega^2 f_s + (\kappa_h^2 - 2i\kappa_{sc}\partial_x) f_t &= S(x), \\ \partial_x^2 f_t - \kappa_\omega^2 f_t - (\kappa_h^2 - 2i\kappa_{sc}\partial_x) f_s &= 0, \end{aligned} \quad (\text{S11})$$

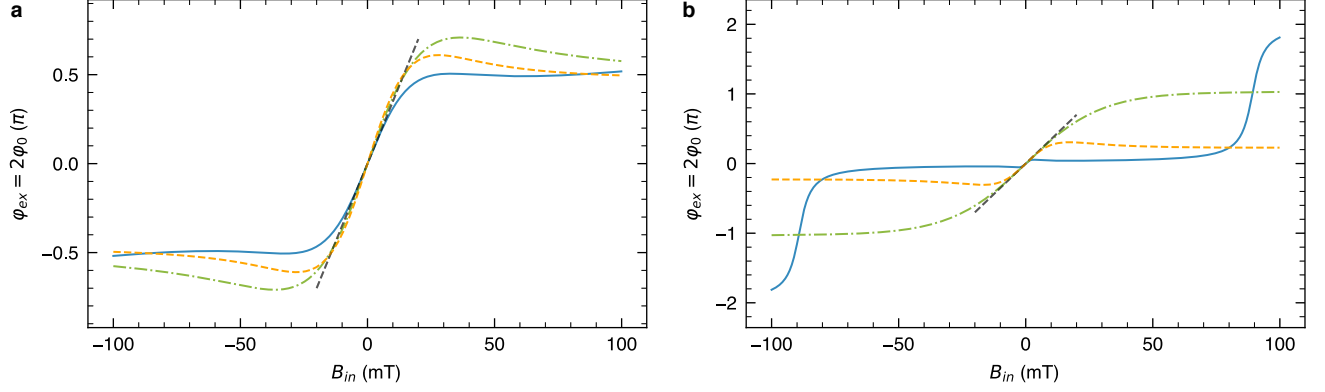


FIG. S5. **Theoretical model of the extrinsic anomalous phase.** The dependence of the extrinsic anomalous-phase on the magnetic field applied in y direction (B_{in} at $\theta = \pi/2$) for a) different temperatures, with $\alpha \simeq 0.24 \text{ eV \AA}$ and for b) different values of α , with $T \simeq 10 \text{ mK}$. In a), the solid blue line coincides with the one shown in Fig. 3a of the main text, with $T \simeq 25 \text{ mK}$ and $g_s \simeq 12$. For the dashed orange line, we choose $T \simeq 10 \text{ mK}$ and $g_s \simeq 5$, and for the dashed-dotted line, $T \simeq 5 \text{ mK}$ and $g_s \simeq 2$. In b), the solid blue line corresponds to $\alpha \simeq 0.1 \text{ eV \AA}$ and $g_s \simeq 37$, the dashed orange line to $\alpha \simeq 0.18 \text{ eV \AA}$ and $g_s \simeq 7$, and the dashed-dotted green line to $\alpha \simeq 0.4 \text{ eV \AA}$ and $g_s \simeq 3$. In both a) and b), the dashed grey line corresponds to the measured slope at low fields.

with

$$S(x) = \gamma f_{\text{BCS}} \left[\Theta \left(x - \frac{L}{2} \right) e^{i\frac{\varphi}{2}} + \Theta \left(-x - \frac{L}{2} \right) e^{-i\frac{\varphi}{2}} \right], \quad (\text{S12})$$

$\kappa_\omega^2 = \frac{2|\omega|}{D}$, $\kappa_h^2 = \frac{2\hbar}{\hbar D}$, and φ is the phase difference between these two Al leads. After a cumbersome but straightforward procedure, we solve Eq. (S11) for continue and finite $f_{s,t}$. From the knowledge of the singlet and triplet components one determines the Josephson current as follows [2]:

$$j(x) = \frac{\pi \sigma_D T}{e} \sum_{\omega} \text{Im} \{ f_s^* \partial_x f_s - f_t^* \partial_x f_t - i \kappa_{\text{sc}} (f_s^* f_t + f_s f_t^*) \}. \quad (\text{S13})$$

The resulting current can be written as $j = I_c \sin(\varphi + \varphi_0)$, with the anomalous-phase given by:

$$\varphi_0 = \arctan \left\{ \frac{\sum_{\omega} \text{Im} \left\{ f_{\text{BCS}}^2 e^{-qL} \frac{\sinh(\kappa_{\text{sc}} L) (q^2 + \kappa_{\text{sc}}^2) + 2q \kappa_{\text{sc}} \cosh(\kappa_{\text{sc}} L)}{q(q^2 - \kappa_{\text{sc}}^2)^2} \right\}}{\sum_{\omega} \text{Re} \left\{ f_{\text{BCS}}^2 e^{-q^* L} \frac{\cosh(\kappa_{\text{sc}} L) (q^{*2} + \kappa_{\text{sc}}^2) + 2q^* \kappa_{\text{sc}} \sinh(\kappa_{\text{sc}} L)}{q^*(q^{*2} - \kappa_{\text{sc}}^2)^2} \right\}} \right\}, \quad (\text{S14})$$

where $q^2 = \kappa_\omega^2 + \kappa_{\text{sc}}^2 - i\kappa_h^2$. In order to compare with the experimental data, we assume a Rashba-like SOC and use the expression derived in Ref. [2] for the spin-charge coupling parameter, namely $\kappa_{\text{sc}} = 2\tau\alpha^3 m^{*2}/\hbar^5$. By using typical values for the parameters of a InAs/Al system: $\xi_0 \simeq 100 \text{ nm}$, $\Delta \simeq 150 \mu\text{eV}$, $m^* = 0.023 m_e$, $T \simeq 25 \text{ mK}$, $g_s \simeq 12$, and $\alpha \simeq 0.24 \text{ eV \AA}$, we find the $\varphi_0(B_{in})$ dependence corresponding to the one shown in Fig. 3a of the main text. We see that our model provides a good qualitative explanation of the two main observed features. Namely, the linear increase of φ_0 for small fields and a kind of saturation at $\varphi_0 \approx \pm 0.5\pi$.

In Fig. S5, we show different $\varphi_0(B_{in})$ curves obtained from our general expression (S14). Whereas for small fields the experimental slope (dashed grey line) can be obtained from different values of the parameters, the behaviour of φ_0 at larger fields depends strongly on these parameters.

Indeed, it is important to emphasize that the saturation value at $\varphi_0 \approx \pm 0.5\pi$ is not an universal property of the phase-battery. This value depends on the intrinsic properties of the system. In particular, larger values of the SOI α leads to larger values of φ_{ex} at values of the field larger than those accessed in the experiment. This is shown in Fig. (S5)b, where we plot the $\varphi_0(B_{in})$ dependence for different values of α , with $T \simeq 10 \text{ mK}$. As in Fig. (S5)a, we change the g_s value to maintain the experimental slope in the low-field region. The linear behavior for the low-field region is shared by all the $\varphi_0(B_{in})$ curves, as shown in Fig. (S5). In this regime, we can thus find the slope value by linearizing Eq. (S14):

$$\varphi_0 \simeq C_1 B_{in} + O(B_{in}^3), \quad (\text{S15})$$

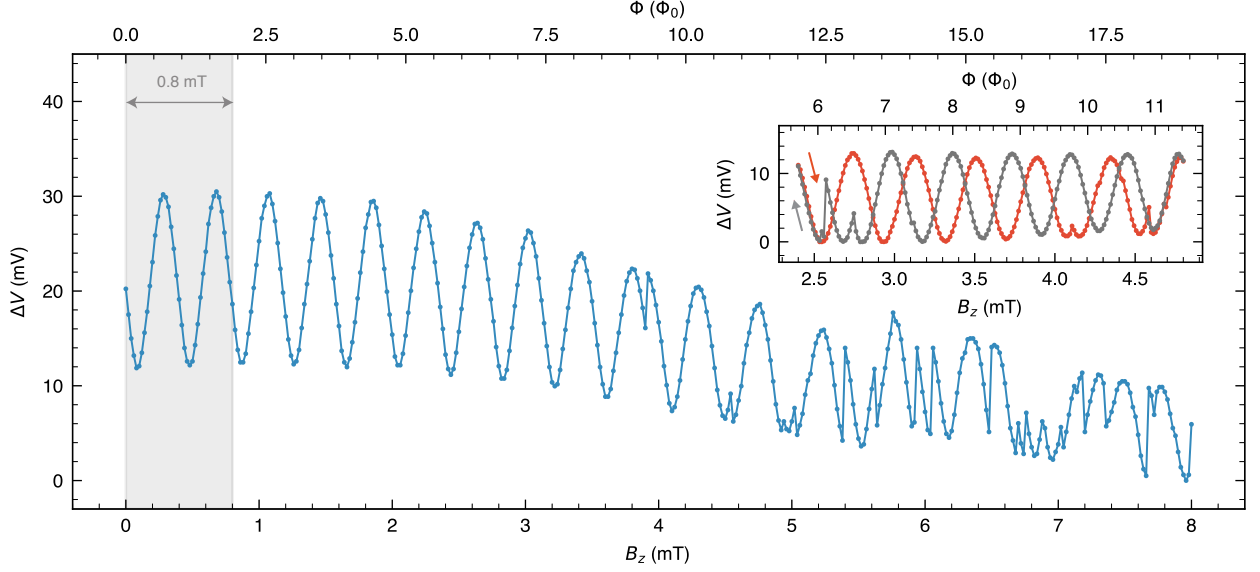


FIG. S6. **Fluxons induced phase shifts at high B_z .** Voltage drop $\Delta V(B_z)$ across the SQUID for $I_{sd} = 1 \mu\text{A}$ versus applied magnetic field B_z up to 8 mT recorded at $T = 100 \text{ mK}$. The grey area indicated in the plot (corresponding to $0 \leq B_z \leq 0.8 \text{ mT}$) is the one used to track and evaluate the induced phase shift in our interferometer. For $B_z \gtrsim 3 \text{ mT}$ abrupt jumps in the phase start to appear due to trapped fluxons piercing the SQUID area. Inset: back (gray) and forth (red) traces at high B_z in the same conditions as before show an hysteretic behavior which is expected for fluxons pick-up.

with $C_1 \simeq 0.035 \pi/\text{mT}$, which is in agreement with the value extracted from the experiment.

VI. TRIVIAL MECHANISMS TO INDUCE PHASE SHIFTS

Trivial hypotheses, alternative to the anomalous φ_0 effect, have been also considered for the for the generation of a hysteretic phase shift: trapped magnetic fluxes and Abrikosov vortices.

- Trapped magnetic fluxes can be observed in superconducting loops with a non negligible ring inductance L and, more precisely, for a screening parameter $\beta_L = \frac{2\pi L I_c}{\Phi_0} \gtrsim 1$, with I_c being the critical current of a single junction [22]. This indeed can lead to a hysteretic behavior due to the presence of a circulating current in the ring. For our interferometer we estimated $\beta_L \lesssim 10^{-2}$ ($I_c \sim 300 \text{ nA}$ and $L \sim 10 \text{ pH}$ [17]) that is very unlikely to induce any magnetic hysteresis. Still, if circulating currents are present, hysteretic jumps should be sharp, periodic and visible even at low B_z . The absence of any hysteretic behavior at low magnetic field is further confirmed by the continuous interference patterns shown in Figs. 1e and 1f.
- Abrikosov vortices, also known as fluxons, can be often induced in type-II superconductors – like the thin Al film used in our SQUID devices – when an out-of-plane magnetic field is applied. To avoid vortex intrusion into the ring surface, which might induce a parasitic phase shift, we limit our out-of-plane component to $|B_z| < 0.8 \text{ mT}$, which guarantees the absence of any fluxon. Indeed, upon the application of a larger field $B_z \gtrsim (3 - 4) \text{ mT}$, also in our case abrupt phase shifts appear with a density that increases by increasing B_z , as shown in Fig. S6. This is what is expected for fluxons pinning in the Al, i.e., stochastic and abrupt events providing a discrete jump of the phase [25]. Notice also the hysteretic behavior expected for fluxon inclusion, which is underlined in the inset of the figure showing a local back and forth measurement.

With respect to the in-plane magnetic fields, the thickness of the Al film (thinner than the superconducting coherence length) ensures the complete penetration of the magnetic field, and thereby the absence of generated fluxons. This is consistent with the lack of any stochastic shift upon the application of B_{in} .

VII. SUPPLEMENTARY DEVICE MEASURED

In this section we repeated the same magnetic characterization of the Josephson phase battery shown in Fig. 2 and 3 of the main text, performed on a different device to demonstrate the high reproducibility of the effect, apart sample-specific details. Notice that the behaviour of φ_{tot} and φ_{int} (Fig. S7) is qualitatively similar, but with a smaller total phase shift of $\sim 0.4\pi$ stemming for a weaker exchange interaction induced by the unpaired-spin. Moreover the angle dependence of $\varphi_{ex}(\theta)$ shown in Fig. S8 is in very good agreement with the evolution observed in Fig. 2 and expected from the model presented in Section V.

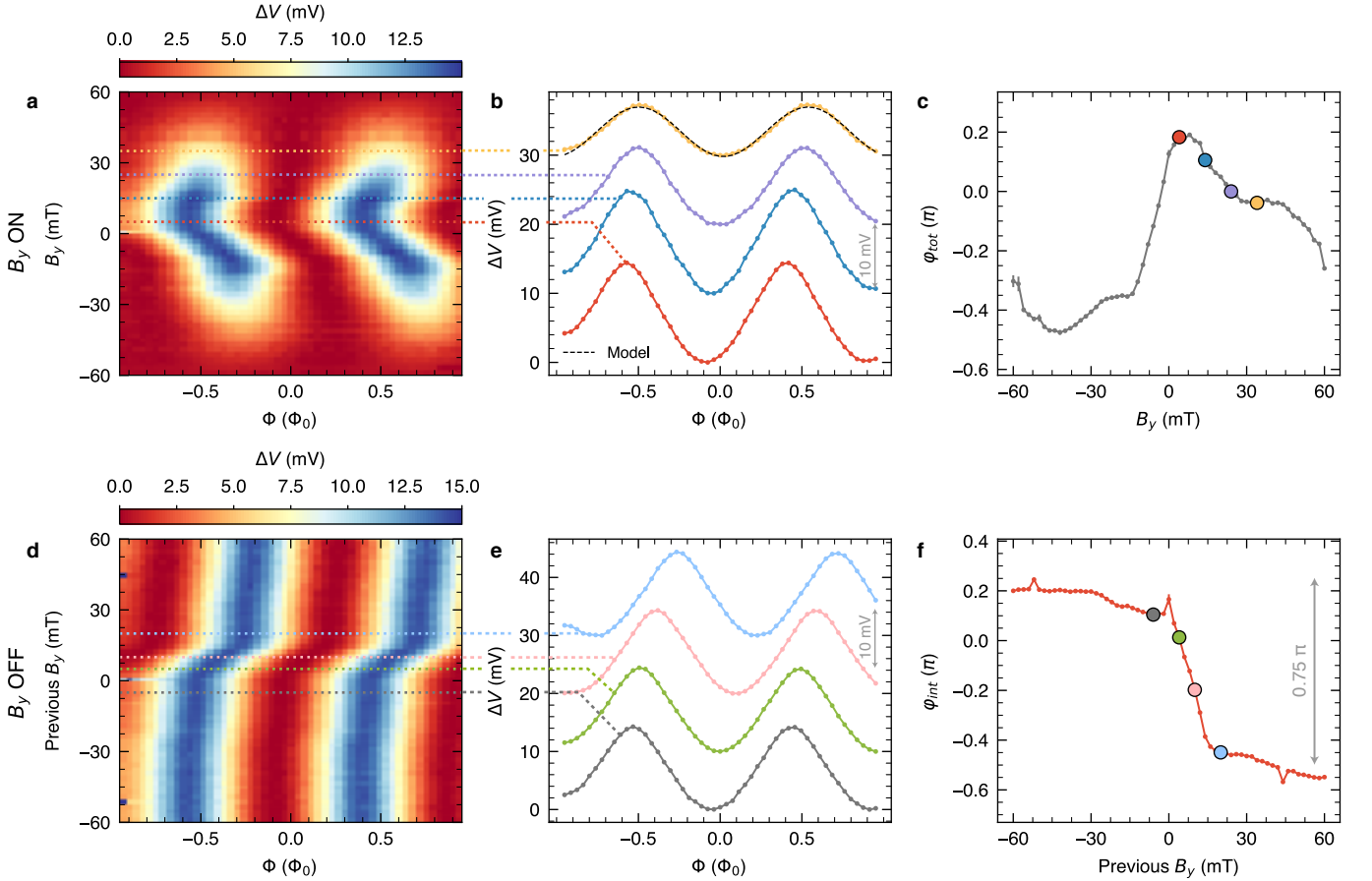


FIG. S7. **Charging loops of the Josephson phase battery (second device).** **a**, Voltage drop $\Delta V(\Phi)$ at constant current bias $I = 1 \mu\text{A}$ versus in-plane magnetic field B_y applied orthogonal to the nanowire axis. At large $|B_y|$, the amplitude of $\Delta V(\Phi)$ is lowered due to the suppression of superconductivity inside the wire. Each trace is vertically offset for clarity. **b**, Selected traces $\Delta V(\Phi)$ extracted from **a** for different B_y . Data are vertically offset for clarity. **c**, Extracted phase shift φ_{tot} from the curves in **a**. **d**, Color plot of the persistent voltage drop $\Delta V(\Phi)$ measured at $B_y = 0$ after the magnetic field was swept to the values shown on the y -axis. **e**, Selected traces $\Delta V(\Phi)$ corresponding to the cuts in **d**. **f**, Intrinsic phase shift φ_{int} extracted from **d**. φ_{int} stems from the ferromagnetic polarization magnetic impurities. All data were recorded at 30 mK of bath temperature.

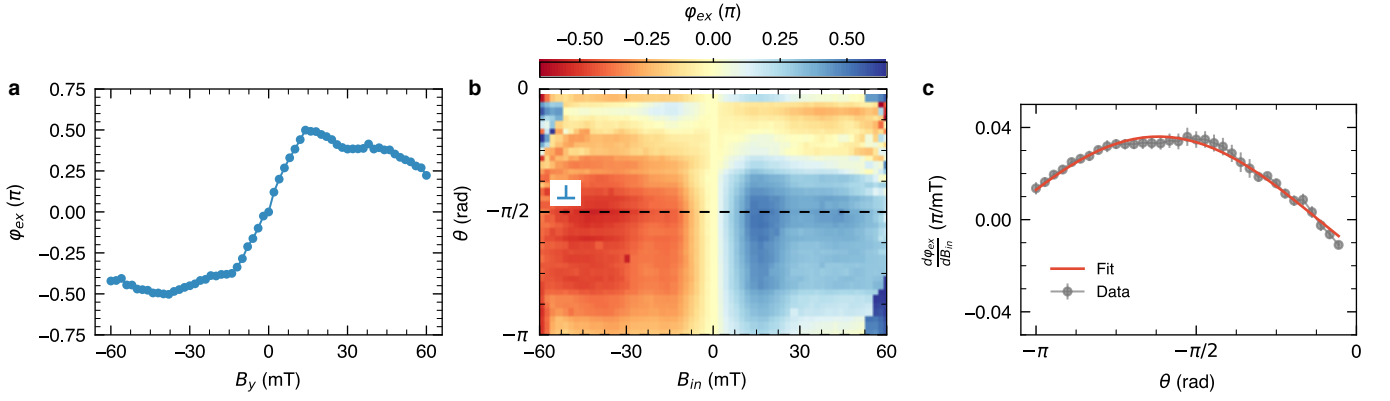


FIG. S8. **Vectorial symmetry of the anomalous phase φ_0 (second device).** **a**, Dependence of the extrinsic anomalous phase φ_{ex} on B_y . **b**, Evolution of the anomalous phase φ_{ex} on θ and B_{in} . **c**, $d\varphi_{ex}/dB_{in}$ versus θ together with a sinusoidal fit (red curve) from Eq. (S15). The slope has been evaluated by a linear fit of the data in **b** for $|B_{in}| < 10$ mT. The error bar is the RMS of the fit. All the data were recorded at 30 mK of bath temperature.

VIII. LOW MAGNIFICATION SEM IMAGE OF THE DEVICE

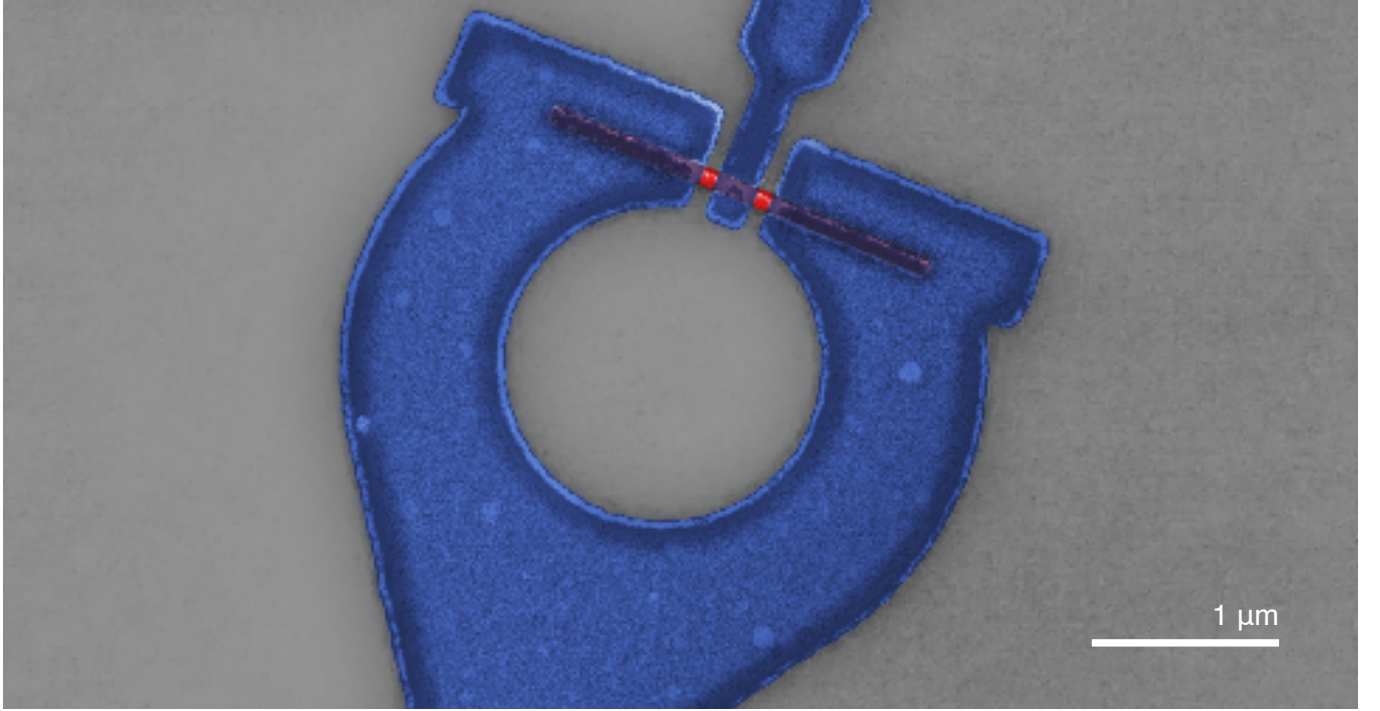


FIG. S9. **Low magnification SEM image of the device.** As shown in Fig. 1c of the main text.

-
- [1] Gomes, U. P., Ercolani, D., Zannier, V., Beltram, F. & Sorba, L. Controlling the diameter distribution and density of InAs nanowires grown by Au-assisted methods. *Semicond. Sci. Technol.* **30**, 115012 (2015).
 [2] Wallentin, J. & Borgström, M. T. Doping of semiconductor nanowires. *Journal of Materials Research* **26**, 2142–2156 (2011).

- [3] Iorio, A. *et al.* Vectorial Control of the Spin–Orbit Interaction in Suspended InAs Nanowires. *Nano Lett.* **19**, 652–657 (2019).
- [4] Rogachev, A. *et al.* Magnetic-Field Enhancement of Superconductivity in Ultranarrow Wires. *Physical Review Letters* **97**, 137001 (2006).
- [5] Sapkota, K. R., Maloney, F. S. & Wang, W. Observations of the Kondo effect and its coexistence with ferromagnetism in a magnetically undoped metal oxide nanostructure. *Phys. Rev. B* **97**, 144425 (2018).
- [6] Kondo, J. Resistance Minimum in Dilute Magnetic Alloys. *Prog. Theor. Phys.* **32**, 37–49 (1964).
- [7] Bid, A., Bora, A. & Raychaudhuri, A. K. Temperature dependence of the resistance of metallic nanowires of diameter ≥ 15 nm: Applicability of bloch-grüneisen theorem. *Phys. Rev. B* **74**, 035426 (2006).
- [8] Goldhaber-Gordon, D. *et al.* From the Kondo Regime to the Mixed-Valence Regime in a Single-Electron Transistor. *Phys. Rev. Lett.* **81**, 5225–5228 (1998).
- [9] Parks, J. J. *et al.* Mechanical control of spin states in spin-1 molecules and the underscreened kondo effect. *Science* **328**, 1370–1373 (2010).
- [10] Mallet, F. *et al.* Scaling of the Low-Temperature Dephasing Rate in Kondo Systems. *Phys. Rev. Lett.* **97**, 226804 (2006).
- [11] Costi, T. A. *et al.* Kondo Decoherence: Finding the Right Spin Model for Iron Impurities in Gold and Silver. *Phys. Rev. Lett.* **102**, 056802 (2009).
- [12] Hamann, D. R. New Solution for Exchange Scattering in Dilute Alloys. *Phys. Rev.* **158**, 570–580 (1967).
- [13] Bergeret, F. S. & Tokatly, I. V. Theory of diffusive φ_0 Josephson junctions in the presence of spin-orbit coupling. *EPL* **110**, 57005 (2015).
- [14] Konschelle, F., Tokatly, I. V. & Bergeret, F. S. Theory of the spin-galvanic effect and the anomalous phase shift φ_0 in superconductors and Josephson junctions with intrinsic spin-orbit coupling. *Phys. Rev. B* **92**, 125443 (2015).
- [15] Buzdin, A. Direct coupling between magnetism and superconducting current in the josephson φ_0 junction. *Phys. Rev. Lett.* **101**, 107005 (2008).
- [16] Clarke, J. & Braginski, A. I. (eds.) *The SQUID handbook* (Wiley-VCH, Weinheim, 2004).
- [17] D’Ambrosio, S., Meissner, M., Blanc, C., Ronzani, A. & Giazotto, F. Normal metal tunnel junction-based superconducting quantum interference proximity transistor. *Applied Physics Letters* **107**, 113110 (2015).
- [18] Golod, T., Rydh, A. & Krasnov, V. M. Detection of the phase shift from a single abrikosov vortex. *Phys. Rev. Lett.* **104**, 227003 (2010).